Engineering stepped edge surface structures of MoS2 sheet stacks to accelerate the hydrogen evolution reaction

Jue Hu,[a] Bolong Huang,[b] Chengxu Zhang,[c,d] Zilong Wang,[a] Yiming An,[a] Dan Zhou,[a] He Lin, [a] Michael K. H. Leung,[c] Shihe Yang[a]*

Two-dimensional molybdenum sulfide is an attractive noble-metal-free electrocatalyst for the hydrogen evolution reaction (HER). Significant efforts have been spent on increasing the number of exposed edge sites. However, little attention has been paid to devising edge surface structures of MoS2 sheet stacks to promote the HER kinetics. Herein we report the first demonstration of significantly enhanced HER kinetics by controllably fabricating a stepped MoS2 surface structure. Vertical arrays of MoS2 sheets terminated with such a stepped surface structure have proved to be an outstanding HER electrocatalyst with overpotential of 104 mV at 10 mA/cm2, exchange current density of 0.2 mA/cm2 and high stability. Experimental and theoretical results indicate that the enhanced electrocatalytic activity of the vertical MoS2 arrays is associated with the unique vertically terminated, highly exposed, stepped surface structure with a nearly thermoneutral H-adsorption energy. This work opens a new avenue to designing and developing layered materials for electrochemical energy application

Introduction

Hydrogen is arguably the cleanest fuels of the future since water is the sole product during its oxidation reaction.[1, 2] The opposite hydrogen evolution reaction (HER) from water can then close the circle, which can power the "hydrogen-based economy". The current challenge is to develop efficient, durable and low cost electrocatalytic materials for HER.[3, 4] Pt-based catalysts are by far the most active ones and thus used as a benchmark for HER, but the high cost and scarcity have greatly hindered their widespread applications.[5, 6] Recently, there have been remarkable advances on the exploitation of earth-abundant transition-metal-dichalcogenides, MoS_2, $MoSe_2$, WS_2, CoS_2, $CoSe_2$, $NiTe_2$, etc., for the noble-metal-free electrocatalysts of HER because of their low cost and high abundance.[7-12] Typical among them is MoS_2, which has a layered-structure with unique physical and chemical properties.[13, 14]

As shown in Figure 1A, the structural unit of a MoS_2 crystal is composed of a Mo layer sandwiched between two S layers through covalent S-Mo-S bonding, and van der Waals force then holds the repeating units together with a layer-to-layer distance of about 0.62 nm, terminating with two types of surfaces: terrace sites on the basal planes and edge sites within the layers. Density function theory (DFT) calculations have elucidated that the MoS_2 edge sites are active for HER because those edge sites hold a near-optimal hydrogen adsorption free energy (ΔG_H is 0.08 eV) for HER, while the basal plane of MoS_2 is catalytically inert (ΔG_H is 2 eV).[15] Subsequent experiments by Jaramillo and co-workers confirmed that the HER activity is indeed linearly proportional to the number of edge sites of the MoS_2 catalyst.[16] Motivated by this understanding, extensive efforts have been devoted to developing MoS_2 nanostructures to maximize the active edge sites, including nanoparticle,[17] nanowire,[18] amorphous film,[19] film with ordered double-gyroid network,[20] nanosheet,[21] and defect-rich nanosheet.[3] However, besides increasing the number of exposed edge sites, little attention has been paid to tailoring the MoS_2 edge surface structure itself for enhancing the HER kinetics. Herein we document the first demonstration of a significant HER enhancement by tailoring a stepped edge surface structure of MoS_2 multilayers with respect to a flat edge surface. We provide an unambiguous interpretation on the HER performance difference in terms of the different H bonding on the stepped edge surface (se-MoS_2) and on the flat edge surface (fe-MoS_2).

More recently, Christopher Chang and coworkers have reported a mimic structure of the triangular active edge site fragments of MoS_2, the active sites for HER.[22] This supports the consensus with high-resolution scanning tunneling microscopy studies that in a MoS_2 layer, Mo-edges stabilized by disulfide ligands are responsible for the HER activity as shown in Figure 1B.[23-25] Following the procedure of Nørskov et al.,[15] we performed DFT calculations to evaluate ΔG_H on flat and stepped Mo-edges which are stabilized by disulfide ligands. To highlight the influence given by adjacent layers, we modelled

a ¼ ML H absorption on one single layer for both the se-MoS_2 and fe-MoS_2 edge surfaces, where the H is going to be adsorbed on one of the S atoms from the two disulfide ligands (S_2^{2-}). ΔG_H is ~0.05 eV for the fe-MoS_2 (Figure 1C), indicating that the flat MoS_2 edge surface is active but a slightly strengthened hydrogen adsorption is still needed to further improve the HER kinetics on the MoS_2 edges. As shown in Figure 1D, and Figure S1-3 and Table S1 in Supplementary Information, the p-orbital levels has larger HOMO-LUMO splitting for se-MoS_2 than fe-MoS_2, showing more charge transfer for a proton-electron exchange for H^+ to bind with S_2^{2-} in se-MoS_2 system. The increased energy interval between the bonding and anti-bonding states of the S p-orbitals and H s-orbitals for stepped edge surface typically leads to a stronger hydrogen binding. Therefore, the stronger hydrogen chemisorption for se-MoS_2 compared with fe-MoS_2 leads to a reduced ΔG_H (~0.02 eV) on the stepped MoS_2 edge surface (Figure 1C). Furthermore, as shown in Figure 1E,F and Figure S4-5 in Supplementary Information, the bonding in the fe-MoS_2 system has an unusual medium ranged ordered (MRO) to long ranged ordered (LRO) p-π resonance with a large component given by the aligned disulfide ligands (S_2^{2-}) through interlayers, while it is weakened or absent in the se-MoS_2 system due to the misaligned p-π orbitals. The weakened MRO and LRO in the se-MoS_2 system will increase the degree of p-electrons localization on S_2^{2-} at the edge sites for enhanced reactivity toward H^+ contact and charge exchange. For analysis details see supporting information. Another point of view on structural relaxation will be discussed below.
Therefore, our DFT calculations suggest a more optimal ΔG_H of the active se-MoS_2 edge surface than that of the fe-MoS_2 edge surface, and thereby a faster HER kinetics. A perfectly designed stepped edge surface terminated MoS_2 sheet array is schematically depicted in Figure 1G, in which the unique vertically terminated, stepped surface structure ensures an optimal hydrogen adsorption energy (ΔG_H is ~0.02 eV); the vertical array would permit ultrafast electron transport and promote HER performance. This approach presented here provides a new insight that we tailor the edge active sites to modulate the performance of HER and should be applicable to generalized transition-metal-dichalcogenide catalysts, by engineering their surface structures.

Experimental

Material synthesis

All chemicals are of analytical grade and were used as received without further purification. Ultrapure deionized water (18.2 MΩ/cm) was used in all experiments. Carbon fiber paper (CFP, HCP020P, Hesen) was first immersed in 98% H_2SO_4 (Sigma-Aldrich) for 1 hour to remove the residual metal on the surface. In a typical synthesis of se-MoS_2 on CFP, 671 mg sodium molybdate dihydrate (>99.5%, Sigma-Aldrich) was dissolved in 40 ml N_2-saturated water. Then 225 mg thioacetamide (>99%, Sigma-Aldrich) was add into the beaker with dissolved sodium molybdate dihydrate solution. After stirring the mixture for half an hour under continuous N_2 flow, the mixed solution was transferred to a 100 ml Teflon vessel, and then one piece of cleaned CFP (2cm × 4cm) was immersed in the mixture. The Teflon vessel was sealed and maintained at 200 ℃ for 2 h in a microwave hydrothermal system (2.45 GHz, Ethos one, Milestone Inc.) with accurately monitoring and controlling the internal temperature within ±5 ℃. Then the reaction mixture was cooled to room temperature at the speed of 20 ℃/min. The product was washed with ultrapure deionized water for several times, and then sonicated for at least 30 min to remove the weakly bonded MoS_2 from the surface, and lastly dried in the vacuum oven at the temperature of 60 ℃. For comparison, r-MoS_2 and fe-MoS_2 samples were synthesized under the same condition and followed the same procedure. The only difference for r-MoS_2 is using conventional hydrothermal process instead of microwave hydrothermal process, and for fe-MoS_2 is adjusting the reaction time as 50 min. The loadings of the as-obtained MoS_2 nanostructure for r-MoS_2, fe-MoS_2 and se-MoS_2 samples which were accurately measured by weighing the dry CFP before and after synthesis process are about 2.1 and 3.6 mg/cm^2 and 3.2 mg/cm^2, respectively.

Characterization

The as-synthesized samples were examined by X-ray powder diffraction (XRD) which was carried out on a Philips PW-1830 X-ray diffractometer with Cu Kα radiation (K=0.15418 nm). Raman spectra were performed using a Raman microscope Renishaw 2000 excited with a 514 nm argon ion laser of 2mm spot size excitation. X-ray photoelectron spectroscopy (XPS) were measured on a Perkin-Elmer model PHI 5600 XPS system with a resolution of 0.3–0.5 eV from a monochromated aluminum anode X-ray source with MoKα radiation (1486.6 eV). The morphology of the as-synthesized samples were determined by using field-emission scanning electron microscopy (FESEM) which was characterized by a JEOL JSM-6700F at an accelerating voltage of 5 kV. Transmission electron microscope (TEM), selected area electron diffraction (SAED) and energy-disperse X-ray spectrum (EDS) were taken with a JEOL-2010 with an acceleration voltage of 200 kV. High resolution transmission electron microscope (HRTEM) images were captured on a JEOL-2010F instrument microscopy at an accelerating voltage of 200 kV. Atomic force microscopy (AFM) samples were measured on Dimension 3100 of Veeco Metrology Group with Si tip. AFM samples are prepared by drop the diluted catalyst suspensions onto silicon wafer. The attenuated total reflection Fourier transform infrared spectroscopy (ATR-FTIR) spectra of dried fe-MoS_2 and seMoS_2 samples were recorded using Vertex 70 spectrometer (Bruker Corporation) in the range of 600–400 cm^{-1}. The spectra were obtained after 256 scans

at 4 cm^{-1} resolution with subtracting the contributions from CO_2 and H_2O (gas). Ultraviolet-visible-near (UV-vis-NIR) absorption spectra were measured using an UV-vis spectrophotometer (UV-2600, SHIMADZU) at the wavelength from 185 nm to 1400 nm. For diffuse reflectance mode, $BaSO_4$ was taken as the reference. The generated gas was confirmed by gas chromatography (GC) analysis and measured quantitatively using a calibrated pressure sensor to monitor the pressure change in the anode and cathode compartment of a H-type electrolytic cell. Gas chromatography (GC) analysis was carried out on GC–7900 (Techcomp Co.) with thermal conductivity detector and argon carrier gas. The Faradic efficiency was calculated by comparing the amount of experimentally quantified gas with theoretically calculated hydrogen.

Electrochemical testing

Electrochemical measurements of the as-synthesized MoS_2 samples were performed with a CHI 760D electrochemistry workstation (Shanghai Chenhua Instrument, Inc.) using a standard three-electrode electrochemical cell with Pt foil and Ag/AgCl as the counter and reference electrode, respectively. For comparison, the electrochemical performance of commercial 40 wt% Pt/C (HISPECTM 4000, Johnson Matthey company, JM) with the loading of 0.05 mg/cm^2 which was prepared in 1 mg/ml ink and dropped on the rotating disk electrode, and then measured on the same condition with the rotating rate of 1600 rpm. Commercial bulk MoS_2 (Powder, Aldrich) with the loading of 3 mg/cm^2 which was prepared in 3 mg/ml ink and brushed on the CFP was also measured under the same measuring conditions. Electrochemically inert tape was used to define the 1 cm^2 electrode area. The electrochemical measurements were all performed at room temperature, and the potential were referenced to that of the reversible hydrogen electrode (RHE). For the RHE calibration, the potential difference between Ag/AgCl and RHE was measured in a cell where Pt foil was used as the working electrode and Ag/AgCl was used as the counter and reference electrodes in a 99.999% pure H_2-saturated 0.5 M H_2SO_4 aqueous solution. During all of the electrochemical measurements, high-purity H_2 is purged into the electrolyte to saturate the electrolyte and to ensure the reversible hydrogen potential. The open circuit potential was recorded from an open circuit potential-time curve. Cyclic voltammograms (CVs) were taken several cycles to bubble away the surface contaminates and at the same time stabilize the catalysts. The polarization curves were obtained by averaging the currents measured during both the positive and negative potential sweeps from -0.9 to -0.2V vs. Ag/AgCl with a scan rate of 5 mV/s in H_2-saturated 0.5 M H_2SO_4 aqueous solution. All the polarization curves were *iR*-corrected, except as otherwise noted. Double layer capacitance (C_{dl}) was estimated by the CV cures at various scan rates in the potential region of 0.1-0.2 V vs. RHE. Electrochemical impedance spectroscopy (EIS) was performed at specific overpotential over a frequency range from 100 kHz to 5 mHz at the amplitude of the sinusoidal voltage of 10 mV. In order to avoid the influence from Pt depositing on the working electrode due to the Pt corrosion during a long time electrochemical testing, stability measurements were performed in a special cell where a frit was used to separate the working electrode from the Pt counter electrode.

Theoretical calculation

We used the CASTEP code to perform our DFT+U calculations.[26] In this framework, we use the rotationally invariant (Anisimov type) DFT+U functional[27] and the Hubbard U parameter self-consistently determined for the pseudized Mo $5d^5$ orbital by our new linear response method.[28] To stabilize the hole states that lie in the S 3p orbitals, we also apply a self-consistently determined Hubbard U potential (method used above) to the S 3p states following the approach of Lany,[29] Morgan et al.,[30] and Keating et al.[31] The geometry optimization used the Broyden-Fletcher-Goldfarb-Shannon (BFGS) algorithm through all calculations. The PBE functional was chosen for PBE+U calculations with a kinetic cutoff energy of 750 eV, with the valence electron states expressed in a plane-wave basis set. The ensemble DFT (EDFT) method of Marzari et al.[32] is used for convergence. Reciprocal space integration was performed using the special k-point (¼, ¼, 0) with Gamma-center-off, which was self-consistently selected for total energy minimization. With this special *k*-point, the total energy is converged to less than $5.0x10^{-7}$ eV per atom. The Hellmann-Feynman forces on the atom were converged to less than 0.001 eV/Å.

Results

Design and fabrication of stepped MoS_2 edge surfaces for HER catalysis

In order to purposely build the stepped edge surface-terminated MoS_2 (se-MoS_2) catalyst, we turned to the microwave hydrothermal process. Compared to the conventional hydrothermal route, the microwave hydrothermal route involves direct interactions of microwave with the molecules, atoms and ions, resulting in a more homogeneous and rapid heat-up process.[33] This may help in producing metastable structures such as the above-mentioned stepped edge surface terminated MoS_2 sheet arrays. As shown in Figure 2-3, and Figure S6-10 in Supplementary Information, the morphologies of the microwave hydrothermal-synthesized fe-MoS_2 and se-MoS_2, which display an ordered and vertically aligned sheet structure on carbon fiber paper (CFP) substrate, are quite different from that of the conventional hydrothermal-grown random arranged MoS_2 (r-MoS_2). We believe that the growth mechanism of the MoS_2 layers involve mainly two steps: (1) formation and condensation of suboxide (MoO_{3-x}) species onto the growth substrate, and (2) sulfidization of the suboxide species to

generate the MoS_2 nanostructure.[34] Compared with the r-MoS_2 with a random arranged flower-like morphology, it is obvious that the microwave hydrothermal-grown fe-MoS_2 and se-MoS_2 exhibited a complete and uniform coverage of MoS_2 nanosheets on CFP, indicating the generation of abundant and uniformly distributed reactive seeds covalently bonded onto the CFP surface. It can be seen from Figure S11 that the MoS_2 materials grown on Ti plate and carbon cloth substrates by the same microwave hydrothermal process also show a complete and uniform coverage of MoS_2 nanosheets with an ordered and vertically aligned sheet structure. This establishes the microwave activation as a powerful synthetic route for generating highly homogeneous and fully covered nanostructures on the substrate surface.

TEM images have confirmed the layer-like structure of all the r-MoS_2, fe-MoS_2 and se-MoS_2 samples. The distribution of the Mo and S elements in MoS_2 sheets demonstrated a uniform composition of MoS_2 in all of the r-MoS_2, fe-MoS_2 and se-MoS_2 samples (Figure S13-15 in Supplementary information). The insets in Figure 2C, 3C, Figure S6C and S16 show the corresponding selected-area electron diffraction (SAED) patterns which clarify the same polycrystalline structure for all of the as-synthesized MoS_2 catalysts, and shows strong ring patterns of (100), (103), (110) and (200) planes of MoS_2 crystal. The TEM images for both the fe-MoS_2 and se-MoS_2 samples clearly show the S-Mo-S layers with a layer-to-layer spacing of 0.65 nm, corresponding to the (002) facets of MoS_2 crystal. However, besides the flower-like morphology, the circle-like nanotube and flat-floor morphologies were also observed from the TEM images of the r-MoS_2 sample (Figure S12). Since the surface energy of the MoS_2 edge sites is almost 2 orders of magnitude larger than that of the terrace sites, the interfacial energy between MoS2 and substrate for vertical MoS_2 structure is much smaller than the horizontal structure. Ultimately, the competition between the surface energy and interfacial energy of the MoS_2 structure determines the preferred growth orientation.[35] In the sulfurization step of MoS_2 growth, the MoS_2 layer orientation was seriously affected by the seed layer continuity and sulfurization conditions. It was observed that when continuous and thick seed layers underwent sulfurization, growth of vertically aligned structure was energetically preferable to the growth of large-area horizontal structure because the strain energy induced by horizontal growth can be released by the expansion in vertical direction.[36] Therefore, the generation of fully covered and uniformly distributed seed layers in the microwave hydrothermal synthesis should be beneficial for growing the vertically aligned structure. Moreover, the microwave hydrothermal technique can provide rapid heating, accelerated reaction kinetics, and thus enhanced sulfurization rates. In a rapid sulfurization process, the chemical conversion occurs much faster than the sulfur diffusion, thereby making sulfur diffusion as the rate-limiting process.[37] Therefore, MoS_2 layers which are perpendicular to the substrate were generated for the microwave hydrothermal synthesized fe-MoS_2 and se-MoS_2 samples due to the much faster sulfur diffusion along the layers through van der Waals gaps than across the layers. Our result is in accordance with the previous reports on the growth of MoS_2 and $MoSe_2$ by the rapid sulfurization or selenylation, in which the MoS_2 and $MoSe_2$ structure also adopted a vertical orientation in certain circumstances.[8, 37]

The microwave hydrothermal etching, which was proved to be an effective way to obtain a step-terrace structure for $SrTiO_3$ and Nb:$SrTiO_3$ materials, may also act as a scissor tailoring the MoS_2 edge structure.[38, 39] It is worth noting that the crystal fringes along the edge are stepped for the se-MoS_2 sample, while the edges for fe-MoS_2 are flat. The stepped edge surface of MoS_2 layers which are attributed to the uneven length of the S-Mo-S layer in the se-MoS_2 sheet, were formed when prolong the reaction time, indicating the slight etching effect in the MoS_2 growth process. To investigate the structural evolution process from flat edge surface to stepped edge surface of MoS_2 sheets, the products at reaction time of 40 min, 50 min, 90 min and 120 min were collected, as shown in Figure S17-18. When the reaction time was 40 min, MoS_2 nanosheets began to grow on the CFP substrate and unsulfurized molybdenum suboxide seed layer could still be seen (Figure S17). When the reaction time is extended to 50 min, sulfurization step was completed and vertically aligned MoS_2 layers show flat edge surface (Figure S18D). When prolonging the reaction time to 90 min, MoS_2 layers with slightly etched edges could be seen (Figure S18E). On further prolong the reaction time to 120 min, the MoS_2 layers were further etched and well-defined stepped-edge surface were obtained (Figure S18F). The AFM height profile of fe-MoS_2 (Figure S19) shows a smooth decrease at the MoS_2 edges. However, the height profiles of se-MoS_2 (Figure 2E-G and Figure S19) exhibit several height platforms at the edges and the distance between two of the platforms is about 0.65 nm which is in good agreement with the thickness of one MoS_2 layer, confirming the stepped edge surface-terminated structure of se-MoS_2.

All the X-ray diffraction (XRD) peaks of r-MoS_2, fe-MoS_2 and se-MoS_2 catalysts (Figure 3D) can be indexed to 2H MoS_2 (JCPDS: 75-1539), indicating the successful synthesis of the 2H MoS_2 crystalline for all the MoS_2 samples. It is noteworthy that the peak position of MoS_2 (002) for r-MoS_2, fe-MoS_2 and se-MoS_2 samples are shifted to lower angle relatively to commercial MoS_2, indicating a slight lattice expansion of the MoS_2 (002) plane (6.5 Å) in the MoS_2 crystal structure, which is consistent with the TEM analysis.[40, 41] The Raman spectra as shown in Figure 3E for all the MoS_2 samples exhibited two distinct peaks at ~403 cm^{-1} referred to the out-of-plane Mo-S phonon mode (A_{1g}) and at ~379 cm^{-1} corresponded to the in-plane Mo-S phonon mode ($E_{2g}{}^1$) of typical MoS_2 layer structure.[37] The relatively high intensity of the A_{1g} mode for fe-MoS_2 and se-MoS_2 suggests the edge-terminated structure for the vertically aligned MoS_2 sheet arrays, which is in consistent with the SEM and TEM observations.[42]

The infrared spectra of fe-MoS_2 and se-MoS_2 (Figure S20) show intense characteristic bands of edge-terminated disulfide ligands at 508 and 543 cm^{-1} due to the v(S—S) vibrations.[43] For all of the as-synthesized MoS_2 catalysts, the XPS S 2*p* spectrum can be fitted with two distinct doublets ($2p_{3/2}$ and $2p_{1/2}$) (Figure 3F): one doublet at about 162.3 ± 0.2 eV and 163.5 ± 0.2 eV, which reflects the terminal S_2^{2-} or S^{2-} ligands, and the other doublet at about 163.1 ± 0.2 eV and 164.3 ± 0.2 eV, which reflects the apical S^{2-} ligands of the MoS_2 layer structure.[9, 44] The ratios of the lower binding-energy doublet (terminal S_2^{2-} or S^{2-} ligands) to the higher binding-energy doublet (apical S^{2-} ligands) for se-MoS_2 and fe-MoS_2 samples are estimated to be 4.61 and 4.08, by integrated intensities of the S $2p_{3/2}$ peak, respectively, which is much higher than that of the r-MoS_2 sample (2.65) confirming the HER beneficial edge-terminal structure on the fe-MoS_2 and se-MoS_2 surface. In addition, the UV-Vis-NIR spectra of as-synthesized se-MoS_2 are principle consistent with the theoretical time-dependent density functional theory (TDDFT) calculated excitation spectra of the disulfide ligands terminated MoS_2 edges (Figure S21). The broad peak shown by our calculations at the 330 nm and 530 nm are also agreed well with experimental spectra of fe-MoS_2 and se-MoS_2. Therefore, as strongly confirmed by the morphology, AFM height and chemical structure analyses, stepped (se-MoS_2) and flat (fe-MoS_2) edge surface-terminated MoS_2 nanosheet arrays were well designed and synthesized. Figure 2A shows the schematic illustration of the morphology for the se-MoS_2 catalyst deduced from the morphology and chemical structure analyses. The as-showed stepped edge surface-terminated structure which can adjust the electronic structure of the MoS_2 edges for H adsorption and the vertically aligned S-Mo-S layers which ensures an ultrafast electron transport from the carbon fiber paper substrate to MoS_2 edges within one S-M-S may be benefit for improving the HER kinetics.

Insights into the HER kinetics with different edge surface structures of MoS_2

As shown in Figure 4A, fe-MoS_2 gives a low overpotential of 142 mV at 10 mA/cm^2. With se-MoS_2, the HER activity was further boosted with the overpotential as low as 104 mV at the current density of 10 mA/cm^2. As shown in Figure 4B, the HER exchange current density (j_0) for the r-MoS_2, fe-MoS_2 and se-MoS_2 catalysts from the Tafel plots by extrapolation method are 0.04, 0.13 and 0.20 mA/cm^2, respectively. The Tafel slopes of r-MoS_2, fe-MoS_2, se-MoS_2 and commercial Pt/C catalysts were determined to be 121, 69, 59 and 34 mV/dec, respectively. The Tafel slope of the commercial Pt/C catalyst (34 mV/dec) agrees well with the values in the literature.[5, 45] The Tafel slop of r-MoS_2 catalyst is 121 mV/dec, close to the theoretical value of 118 mV/dec (4.6RT/F), indicating that the Volmer step is the rate-determination step on r-MoS_2 catalyst surface. On the other hand, the Tafel slope for fe-MoS_2 and se-MoS_2 catalysts are intermediated between 39 (4.6RT/3F) and 118 mV/dec, indicating that the charge transfer step (Heyrovsky or Volmer step) is the rate determining step in HER for the fe-MoS_2 and se-MoS_2 catalysts.[46] The smaller Tafel slope of 59 mV/dec was obtained for se-MoS_2 catalyst suggesting a faster proton discharge kinetics of se-MoS_2 than that of fe-MoS_2. This was confirmed by the electrochemical impedance spectroscopy (EIS). In all the Nyquist plots (Figure 4C and Figure S22), a semicircle was observed in the low frequency regime, which is dominated by the surface exchange process of hydrogen and intermediate in HER.[47] There is no Warburg impedance indicating that mass transport is rapid enough so that the reaction is kinetically controlled.[48] Thus the equivalent circuit shown in Figure 4C was used to model the catalytic system, where R_s is attributed to the uncompensated series resistance, constant-phase element (CPE) refers to the double-layer capacitance under HER conditions, and R_{ct} represents the charge transfer resistance in HER. The charge-transfer Tafel slope (Figure 4C) was derived from the linear fit of the plot of log R_{ct} versus overpotential, and is 56 mV/dec for the se-MoS_2 catalyst. This value is very close to the Tafel slope obtained from the voltammetric data (59 mV/dce) reflecting not only a charge transfer rate determining step but also a quick electron transfer feature of the se-MoS_2 catalyst in HER.[19] The Nyquist plots at the overpotential of 200 mV (Figure S22B) show that the se-MoS_2 catalyst has the smallest charge transfer resistance (R_{ct}) of only 2.7 Ω, indicating the ultrafast Faradaic process and thus a superior HER kinetics. The practical hydrogen production rate in Figure S23 agreed well with the theoretical value revealing that an approximately 100% of Faradic efficiency was attained.

The high density of the active sites on the surface can also be demonstrated by the high electrochemical surface area (ECSA) of the vertically aligned MoS_2 sheet array by testing the electrochemical double layer capacitances (C_{dl}).[49] Although, there is a concern that the double layer capacitance involves the entire surface of the MoS_2 while only part of surface sites, for example the edge sites, are HER active, the C_{dl} method is still a method of choice to evaluate the ECSA of transition metal compounds.[49-52] In order to facilitate comparison with the literature results, we also opted to use the double layer capacitances to estimate the electrochemical surface area for the MoS_2 catalysts. The halves of the positive and negative current density differences at the center of the scanning potential range ($\Delta j_{0.15V}/2$) are plotted versus the scan rate shown in Figure 4D and Figure S24-25. It can be clearly found that the C_{dl} of the fe-MoS_2 (92.8 mF/cm^2) and se-MoS_2 (113.3 mF/cm^2) is about twice higher than that of the r-MoS_2 catalyst (47.7 mF/cm^2) indicating a much higher electrochemical surface area of the vertically aligned MoS_2 sheet arrays. The exchange current density (j_0) values, normalized with the ECSA, are 3.4×10^{-5}, 5.6×10^{-5}, and 7.1×10^{-5} mA/cm^2 for r-MoS_2, fe-MoS_2 and se-MoS_2 catalysts, respectively, indicating a true surface area corrected improvement of HER kinetics for se-MoS_2 catalyst. Turnover frequency (TOF), which is the number of H_2 molecules evolved per second per active site, is a crucial index to evaluate the intrinsic activities of the HER electrocatalysts. The best TOF value reaches 100 H_2 molecules per second (H_2 s^{-1}) at 36 mV for Pt nanoparticles.[53] To further estimate the intrinsic HER

kinetics of the vertically aligned MoS_2 sheet array, we investigated the TOF of the MoS_2 catalysts using the method reported in the literature (see the Supporting Information for the calculation details).[16, 54] The calculated TOF values (Figure S26) of r-MoS_2, fe-MoS_2 and se-MoS_2 catalysts are 0.096, 0.66 and 1.51 H_2 s^{-1}, respectively, at the overpotential of 200 mV, indicating an enhancement of intrinsic HER activity for se-MoS_2 catalyst. For comparison, the TOF values are 0.1 H_2 s^{-1} for the highly active Li-MoS_2 and 1.4 H_2 s^{-1} for molybdenum phosphosulfide ($MoS_{0.94}P_{0.53}$) at the overpotential of 200mV at 0.5 M H_2SO_4, suggesting that the TOF value of se-MoS_2 is among the highest values for noble-metal-free catalysts.[51, 55]

In order to better compare the HER kinetics with the recently reported highly active MoS_2-based catalysts, including amorphous molybdenum sulfides,[19] MoS_2/N-doped CNT,[56] Li-MoS_2/carbon fiber,[51] defect-rich MoS_2[3], double-gyroid MoS_2,[20] Co/Ni-MoS_3 hollow structure,[57] strained vacancy MoS_2[45], edge-terminate MoS_2 film,[37] etc, the overpotentials required for maintaining the HER current density of -10 mA/cm^2 of most active MoS_2-based catalysts were listed, as shown in Figure 4E and Table S3. The HER performance of se-MoS_2 is markedly better than or at least comparable to those of the most active HER electrocatalysts in acidic solutions.

As shown in Figure 4F and Figure S27 in Supplementary Information, over the duration more than 24 hours, the cathodic overpotential required to maintain a cathodic current density 10 mA/cm^2 for se-MoS_2 catalyst decreased from 104 mV to 95 mV, while the cathodic overpotential for Pt/C increased more than 15 mV after 18 hours chronopotentiometry measurement. The XRD pattern and Raman spectrum of se-MoS_2 after electrochemical testing are essentially the same as that of the initial se-MoS_2 (Figure S28), suggesting no obvious structural changes of se-MoS_2 during the HER catalysis. The Mo/S ratios for se-MoS_2 catalyst before and after electrochemical testing are 1:1.92 and 1:1.88, respectively, based on the XPS analysis. The XPS spectra of the Mo 3d region for se-MoS_2 catalyst show strong doublet peaks at 229 eV and 232.1 eV assigned to Mo^{4+} $3d_{5/2}$ and Mo^{4+} $3d_{3/2}$, respectively. The doublet peaks at 232.7 eV and 235.8 eV which are related to Mo^{6+} suggest a small amount of MoO_3 species exist on the se-MoS_2 surface. After electrochemical testing, the intensity of this doublet peaks decreased and new doublet peaks at 230.2 eV and 233.5 eV attributed to MoO_{3-x} generated due to the MoO_3 reduction.[58] Regarding the S 2p signal, it is obvious that there is no difference in the S components of the se-MoS_2 catalyst after more than 24 hours of electrochemical testing (Figure S28). The striking stability of the se-MoS_2 catalyst was further proved by the comparison of the HER performance and morphology at initial time and after different periods of chronopotentiometry measurement. Remarkably, there is no difference in the morphology and ECSA of the se-MoS_2 catalyst after more than 24 hours at -10mA/cm^2 and there is no HER activity decay was observed even after 24 hours chronopotentiometry measurement at -20 mA/cm^2. The superior electrocatalytic activity and the excellent long-term stability of the stepped edge-terminated MoS_2 sheet array (se-MoS_2) catalyst suggest the great promise of using it to fabricate economic-effective and efficient hydrogen evolution catalyst in water electrolysis systems.

Discussion

For the electrocatalysis reactions, the catalysts' activities depend sensitively on the energetics of the interactions between the metal surfaces and the key reaction intermediates, including adsorption, bond making, bond breaking and desorption.[59] It is well known that for a highly active HER catalyst, the free energy of hydrogen adsorption (ΔG_H) should be close to thermoneutral to compromise the reaction barriers of the adsorption and desorption steps.[60] DFT calculations, which are consistent with experimental results, revealed that MoS_2 have an optimal ΔG_H of 0.15 eV and 0.08 eV at the S-edges and S stabilized Mo-edges, respectively, and thus edge sites are active sites for HER, while the basal plane of MoS_2 is catalytically inert.[15, 45, 61] Here, as strongly confirmed by the morphology and chemical structure analyses, flat edge and stepped edge surface-terminated MoS_2 sheet arrays (fe-MoS_2 and se-MoS_2) possess high exposure of active edge sites on the surface, which provides one reason for their boosted HER kinetics.

Besides the abundant exposed edge sites, the catalytic efficacies of the stepped edge surface of the vertically aligned MoS_2 sheet arrays were investigated. Our Hubbard projection calculations indicate that in the se-MoS_2 system, the Mo sites are having less catalytic reactivity than the S sites in hydrogen evolution reactions (Figure S30 in Supplementary Information). We further noticed that the orbitals of HOMO states are mainly localized at the S sites at the Mo-edge including the disulfide ligand S_2^{2-}, while the majority of LUMO states are localized at the Mo sites of the se-MoS_2 system (Figure S31). This indicates the HER reactions of the as-synthesized stepped MoS_2 is coming out at the disulfide ligand sites, in consistent with the combined studies of STM experiments and DFT calculations by Bollinger and coworkers.[62] The PDOS calculations demonstrated a stronger binding energy for se-MoS_2 compared with the fe-MoS_2 system, and thus a lower ΔG_H. Furthermore, we also found when the hydrogen atom contacts onto one of the S atoms of S_2^{2-} and transforms to the relaxed state, the disulfide ligand (S_2^{2-}) has a very flexible switching (or twisting) behavior on the dihedral angles of S-S bond after the hydrogen absorption. It can be seen from the Figure 5 and Figure S32 that the disulfide ligands present double-switch in the stepped se-MoS_2 system while only a local single-switch for the flat fe-MoS_2 system. This indicates that se-MoS_2 system has more local structural relaxation to release the energy in order to reach a more stable H binding state compared with the fe-MoS_2 system, and thus leads to the high HER kinetics of the se-MoS_2 catalysts.

The experimentally measured exchange current density as a function of ΔG_H for stepped and flat MoS_2 edge surfaces were incorporated into a volcano plot in Figure S33. [63] It can be seen that j_0 of MoS_2 with stepped and flat edge surfaces are close to the expected exchange current values in the volcano plot, indicating a good correlation between the theoretical calculations and experimental results.

Conclusion

In summary, we have theoretically elucidated and experimentally verified the effectiveness of our catalyst design strategy, whereby stepped edge surface of MoS_2 acts as a new highly active catalytic structure to accelerate HER kinetics. Given the low overpotential of 104 mV at a current density of 10 mA/cm^2, the high exchange current density at 0.2 mA/cm^2, and the excellent stability, superior to most reported MoS_2-based catalysts as well as the fe-MoS_2 catalyst used as the reference, we expect that our stepped-edge engineering strategy will prove more generally effective for creating catalysts from abundant noble-metal-free layered materials for hydrogen evolution. One of the next goals is to further modify the stepped edge surface terminated layered transition-metal-dichalcogenide catalysts, for example, by incorporating metallic nanomaterials in order to achieve a lower Tafel slope for hydrogen evolution.

Acknowledgements

The authors acknowledge the financial support from the NSFC/Hong Kong RGC Research Scheme (N_HKUST610/14) and the RGC of Hong Kong (GRF No. 16300915). J.H. acknowledges the support by the National Nature Science Foundation of Anhui Province (No. 1508085QA10) and the Youth Innovation Promotion Association of Chinese Academy of Sciences (No. 2015265).

Notes and references

1. D. Strmcnik, M. Uchimura, C. Wang, R. Subbaraman, N. Danilovic, V. van der, A. P. Paulikas, V. R. Stamenkovic and N. M. Markovic, *Nat. Chem.*, 2013, **5**, 300-306.
2. R. Subbaraman, D. Tripkovic, K.-C. Chang, D. Strmcnik, A. P. Paulikas, P. Hirunsit, M. Chan, J. Greeley, V. Stamenkovic and N. M. Markovic, *Nat. Mater.*, 2012, **11**, 550-557.
3. J. Xie, H. Zhang, S. Li, R. Wang, X. Sun, M. Zhou, J. Zhou, X. W. Lou and Y. Xie, *Adv. Mater.*, 2013, **25**, 5807-5813.
4. K. Elbert, J. Hu, Z. Ma, Y. Zhang, G. Chen, W. An, P. Liu, H. S. Isaacs, R. R. Adzic and J. X. Wang, *Acs Catal.*, 2015, **5**, 6764-6772.
5. X. Long, G. Li, Z. Wang, H. Zhu, T. Zhang, S. Xiao, W. Guo and S. Yang, *J. Am. Chem. Soc.*, 2015, **137**, 11900-11903.
6. J. Hu, L. Wu, K. A. Kuttiyiel, K. R. Goodman, C. Zhang, Y. Zhu, M. B. Vukmirovic, M. G. White, K. Sasaki and R. R. Adzic, *J. Am. Chem. Soc.*, 2016, **138**, 9294-9300.
7. D. Kong, J. J. Cha, H. Wang, H. R. Lee and Y. Cui, *Energy Environ. Sci.*, 2013, **6**, 3553-3558.
8. H. Wang, D. Kong, P. Johanes, J. J. Cha, G. Zheng, K. Yan, N. Liu and Y. Cui, *Nano Lett.*, 2013, **13**, 3426-3433.
9. M. R. Gao, J. X. Liang, Y. R. Zheng, Y. F. Xu, J. Jiang, Q. Gao, J. Li and S. H. Yu, *Nat. Common.*, 2015, **6**, 5982-5988.
10. M. Chhowalla, H. S. Shin, G. Eda, L. J. Li, K. P. Loh and H. Zhang, *Nat. Chem.*, 2013, **5**, 263-275.
11. D. Voiry, H. Yamaguchi, J. Li, R. Silva, D. C. B. Alves, T. Fujita, M. Chen, T. Asefa, V. B. Shenoy, G. Eda and M. Chhowalla, *Nat. Mater.*, 2013, **12**, 850-855.
12. H. Tang, K. Dou, C.-C. Kaun, Q. Kuang and S. Yang, *J. Mater. Chem. A*, 2014, **2**, 360-364.
13. A. B. Laursen, S. Kegnaes, S. Dahl and I. Chorkendorff, *Energy Environ. Sci.*, 2012, **5**, 5577-5591.
14. X. Huang, Z. Zeng and H. Zhang, *Chem. Soc. Rev.*, 2013, **42**, 1934-1946.
15. B. Hinnemann, P. G. Moses, J. Bonde, K. P. Jørgensen, J. H. Nielsen, S. Horch, I. Chorkendorff and J. K. Nørskov, *J. Am. Chem. Soc.*, 2005, **127**, 5308-5309.
16. T. F. Jaramillo, K. P. Jorgensen, J. Bonde, J. H. Nielsen, S. Horch and I. Chorkendorff, *Science*, 2007, **317**, 100-102.
17. Y. Li, H. Wang, L. Xie, Y. Liang, G. Hong and H. Dai, *J. Am. Chem. Soc.*, 2011, **133**, 7296-7299.
18. Z. Chen, D. Cummins, B. N. Reinecke, E. Clark, M. K. Sunkara and T. F. Jaramillo, *Nano Lett.*, 2011, **11**, 4168-4175.
19. C. G. Morales-Guio and X. Hu, *Acc. Chem. Res.*, 2014, **47**, 2671-2681.
20. J. Kibsgaard, Z. Chen, B. N. Reinecke and T. F. Jaramillo, *Nat. Mater.*, 2012, **11**, 963-969.
21. X. L. Zheng, J. B. Xu, K. Y. Yan, H. Wang, Z. L. Wang and S. H. Yang, *Chem. Mater.*, 2014, **26**, 2344-2353.
22. H. I. Karunadasa, E. Montalvo, Y. J. Sun, M. Majda, J. R. Long and C. J. Chang, *Science*, 2012, **335**, 698-702.
23. J. V. Lauritsen, J. Kibsgaard, S. Helveg, H. Topsoe, B. S. Clausen, E. Laegsgaard and F. Besenbacher, *Nat. Nano.*, 2007, **2**, 53-58.
24. S. Helveg, J. V. Lauritsen, E. Lægsgaard, I. Stensgaard, J. K. Nørskov, B. S. Clausen, H. Topsøe and F. Besenbacher, *Phys. Rev. Lett.*, 2000, **84**, 951-954.
25. L. P. Hansen, Q. M. Ramasse, C. Kisielowski, M. Brorson, E. Johnson, H. Topsøe and S. Helveg, *Angew. Chem. Int. Ed.*, 2011, **50**, 10153-10156.

26. J. Clark Stewart, D. Segall Matthew, J. Pickard Chris, J. Hasnip Phil, I. J. Probert Matt, K. Refson and C. Payne Mike, *zkri*, 2005, **220**, 567-570.
27. I. A. Vladimir, F. Aryasetiawan and A. I. Lichtenstein, *J. Phys. Condens. Matter.*, 1997, **9**, 767.
28. B. Huang, *J. Comput. Chem.*, 2016, **37**, 825-835.
29. S. Lany and A. Zunger, *Phys. Rev. B*, 2009, **80**, 085202.
30. B. J. Morgan and G. W. Watson, *J. Phys. Chem. C*, 2010, **114**, 2321-2328.
31. P. R. L. Keating, D. O. Scanlon, B. J. Morgan, N. M. Galea and G. W. Watson, *J. Phys. Chem. C*, 2012, **116**, 2443-2452.
32. N. Marzari, D. Vanderbilt and M. C. Payne, *Phys. Rev. Lett.*, 1997, **79**, 1337-1340.
33. M. B. Gawande, S. N. Shelke, R. Zboril and R. S. Varma, *Acc. Chem. Res.*, 2014, **47**, 1338-1348.
34. A. Zak, Y. Feldman, V. Alperovich, R. Rosentsveig and R. Tenne, *J. Am. Chem. Soc.*, 2000, **122**, 11108-11116.
35. L. Fei, S. Lei, W.-B. Zhang, W. Lu, Z. Lin, C. H. Lam, Y. Chai and Y. Wang, *Nat. Commun.*, 2016, **7**.
36. Y. Jung, J. Shen, Y. H. Liu, J. M. Woods, Y. Sun and J. J. Cha, *Nano Lett.*, 2014, **14**, 6842-6849.
37. D. Kong, H. Wang, J. J. Cha, M. Pasta, K. J. Koski, J. Yao and Y. Cui, *Nano Lett.*, 2013, **13**, 1341-1347.
38. F. Ambriz-Vargas, I. Velasco-Davalos, R. Thomas and A. Ruediger, *J. Vac. Sci. Technol. B*, 2016, **34**, 02M101.
39. I. Velasco-Davalos, R. Thomas and A. Ruediger, *Appl. Phys. Lett.*, 2013, **103**, 202905.
40. M. Shao, K. Sasaki and R. R. Adzic, *J. Am. Chem. Soc.*, 2006, **128**, 7408.
41. D. L. Wang, H. L. L. Xin, R. Hovden, H. S. Wang, Y. C. Yu, D. A. Muller, F. J. DiSalvo and H. D. Abruna, *Nat. Mater.*, 2013, **12**, 81-87.
42. M.-R. Gao, M. K. Y. Chan and Y. Sun, *Nat. Common.*, 2015, **6**, 7493-7500.
43. T. Weber, J. C. Muijsers and J. W. Niemantsverdriet, *J. Phys. Chem.*, 1995, **99**, 9194-9200.
44. T. Wang, L. Liu, Z. Zhu, P. Papakonstantinou, J. Hu, H. Liu and M. Li, *Energy Environ. Sci.*, 2013, **6**, 625-633.
45. H. Li, C. Tsai, A. L. Koh, L. Cai, A. W. Contryman, A. H. Fragapane, J. Zhao, H. S. Han, H. C. Manoharan, F. Abild-Pedersen, J. K. Norskov and X. Zheng, *Nat. Mater.*, 2016, **15**, 48-53.
46. J. Durst, A. Siebel, C. Simon, F. Hasche, J. Herranz and H. A. Gasteiger, *Energy Environ. Sci.*, 2014, **7**, 2255-2260.
47. Q. Su, W. Gong, D. Yoon, C. Jacob, Q. Jia, A. Manthiram, A. J. Jacobson and H. Wang, *J. Electrochem. Soc*, 2014, **161**, F398-F404.
48. D. Merki, H. Vrubel, L. Rovelli, S. Fierro and X. Hu, *Chem. Sci.*, 2012, **3**, 2515-2525.
49. C. C. L. McCrory, S. Jung, I. M. Ferrer, S. M. Chatman, J. C. Peters and T. F. Jaramillo, *J. Am. Chem. Soc.*, 2015, **137**, 4347-4357.
50. C. C. L. McCrory, S. Jung, J. C. Peters and T. F. Jaramillo, *J. Am. Chem. Soc.*, 2013, **135**, 16977-16987.
51. H. Wang, Z. Lu, D. Kong, J. Sun, T. M. Hymel and Y. Cui, *ACS Nano*, 2014, **8**, 4940-4947.
52. J. F. Xie, J. J. Zhang, S. Li, F. Grote, X. D. Zhang, H. Zhang, R. X. Wang, Y. Lei, B. C. Pan and Y. Xie, *J. Am. Chem. Soc.*, 2013, **135**, 17881-17888.
53. J. Kibsgaard and T. F. Jaramillo, *Angew. Chem. Int. Ed.*, 2014, **53**, 14433-14437.
54. J. Kibsgaard, T. F. Jaramillo and F. Besenbacher, *Nat. Chem.*, 2014, **6**, 248-253.
55. R. Q. Ye, P. del Angel-Vicente, Y. Y. Liu, M. J. Arellano-Jimenez, Z. W. Peng, T. Wang, Y. L. Li, B. I. Yakobson, S. H. Wei, M. J. Yacaman and J. M. Tour, *Adv. Mater.*, 2016, **28**, 1427-1432.
56. D. J. Li, U. N. Maiti, J. Lim, D. S. Choi, W. J. Lee, Y. Oh, G. Y. Lee and S. O. Kim, *Nano Lett.*, 2014, **14**, 1228-1233.
57. L. Yu, B. Y. Xia, X. Wang and X. W. Lou, *Adv. Mater.*, 2016, **28**, 92-97.
58. D. R. Cummins, U. Martinez, A. Sherehiy, R. Kappera, A. Martinez-Garcia, R. K. Schulze, J. Jasinski, J. Zhang, R. K. Gupta, J. Lou, M. Chhowalla, G. Sumanasekera, A. D. Mohite, M. K. Sunkara and G. Gupta, *Nat. Commun.*, 2016, **7**.
59. D. Strmcnik, K. Kodama, D. van der Vliet, GreeleyJ, V. R. Stamenkovic and N. M. Marković, *Nat. Chem.*, 2009, **1**, 466-472.
60. J. Greeley, T. F. Jaramillo, J. Bonde, I. Chorkendorff and J. K. Norskov, *Nat. Mater.*, 2006, **5**, 909-913.
61. C. Tsai, F. Abild-Pedersen and J. K. Nørskov, *Nano Lett.*, 2014, **14**, 1381-1387.
62. M. V. Bollinger, J. V. Lauritsen, K. W. Jacobsen, J. K. Nørskov, S. Helveg and F. Besenbacher, *Phys. Rev. Lett.*, 2001, **87**, 196803.
63. J. K. Nørskov, T. Bligaard, A. Logadottir, J. R. Kitchin, J. G. Chen, S. Pandelov and U. Stimming, *J. Electrochem. Soc.*, 2005, **152**, J23-J26.

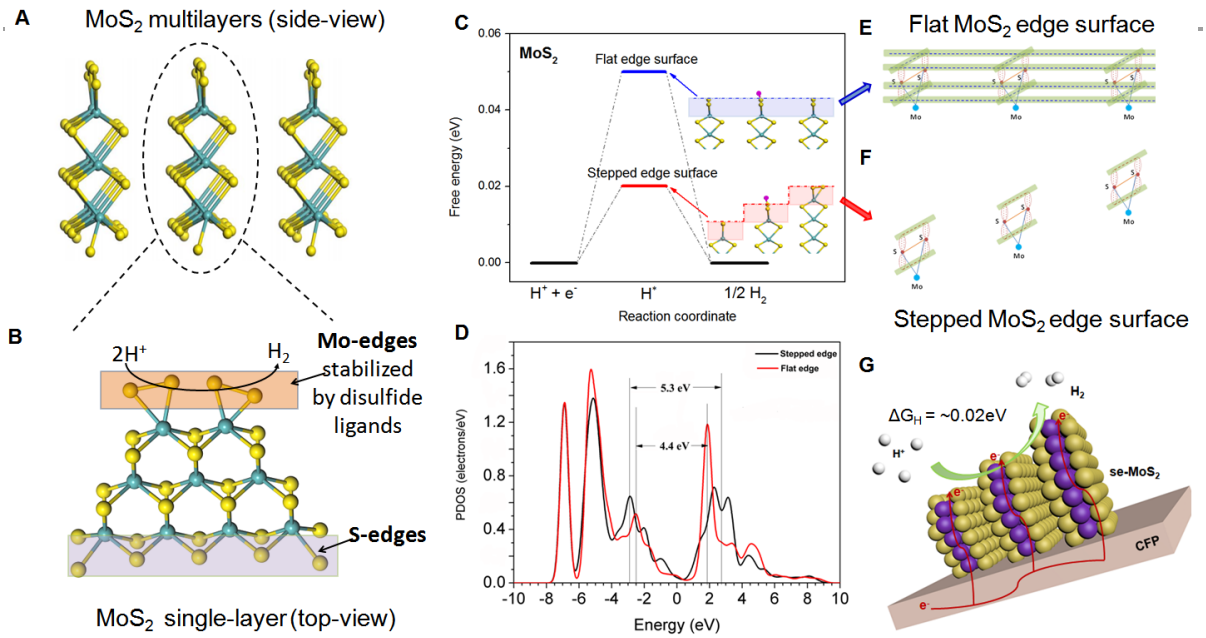

Figure 1 Theoretical calculations revealing effects of the edge surface structure on the HER kinetics of MoS_2. (**A**) Schematic illustration of the MoS_2 multilayers (side-view). (**B**) Schematic illustration of MoS_2 single-layer, where the Mo-edge plane contains disulfide ligands (top-view). (**C**) Free energy diagram for hydrogen adsorption at the stepped and flat MoS_2 edges with one-quarter hydrogen coverage on one of the MoS_2 layers. The molecular structures depicted at the top and bottom of (C) show H adsorption on the fe-MoS_2 and se-MoS_2 edges, respectively. The yellow, dark cyan and violet spheres represent S, Mo and H atoms, respectively. (**D**) Projected p-orbitals density of states (PDOS) of S for the Mo-edge. (**E**) Schematic illustration of the medium ranged ordered (MRO) to long ranged ordered (LRO) p-π resonance in the fe-MoS_2 system. (**F**) Schematic illustration of the weakened to long ranged ordered (LRO) p-π resonance in the se-MoS_2 system. (**G**) Schematic illustration of the designed stepped edge surface terminated MoS_2 sheet array, in which the unique vertically terminated, stepped surface structure ensures optimal hydrogen adsorption energy (ΔG_H is ~0.02 eV) and ultrafast electron transport to the stepped MoS_2 edge surface.

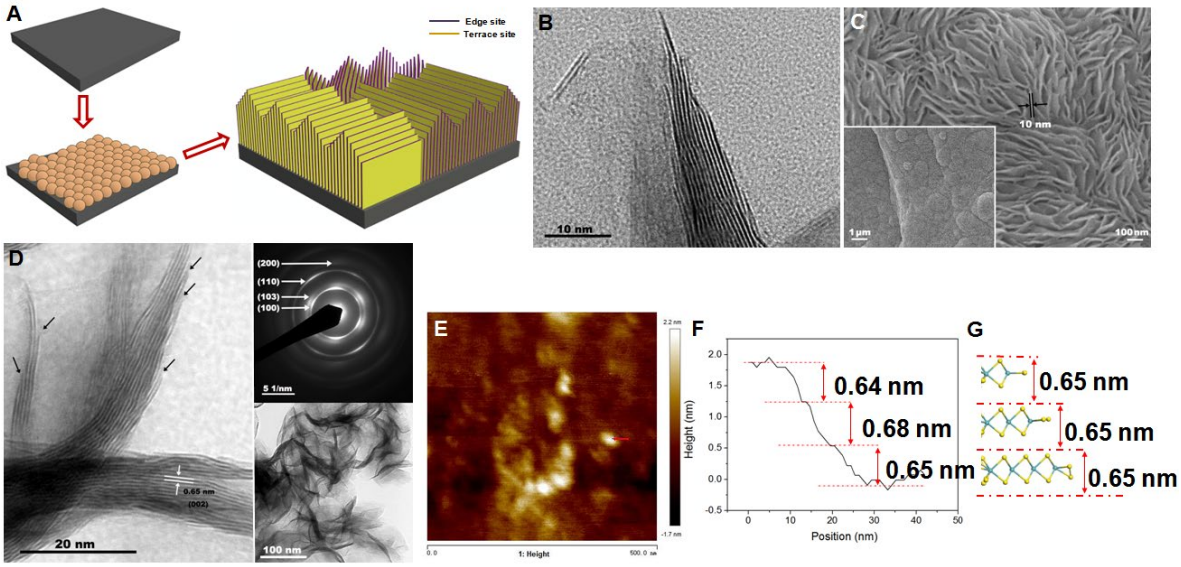

Figure 2 Synthetic strategies for and structure characterizations of the vertically aligned, stepped edge surface terminated MoS_2 sheet arrays (se-MoS_2). (**A**) Synthesis procedure of stepped edge surface-terminated MoS_2 arrays (se-MoS_2) via a microwave hydrothermal method. (**B**) HRTEM image of the se-MoS_2 layers, which clearly shows that crystal fringes of the S-Mo-S layers along the edge are stepped. (**C**) High- and (inset) low-magnification FESEM images of se-MoS_2, suggesting an edge-terminated vertically aligned morphology of MoS_2 nanosheet arrays on the substrate surface. (**D**) High- and low-magnification TEM images and (inset) the corresponding selected-area electron diffraction (SAED) patterns of se-MoS_2. (**E**) AFM topological height image and (**F**) the corresponding height profile of dispersed se-MoS_2. (**G**) The the schematic structure of stepped edge surface-terminated MoS_2 layers, where yellow and dark cyan spheres represent S and Mo atoms, respectively.

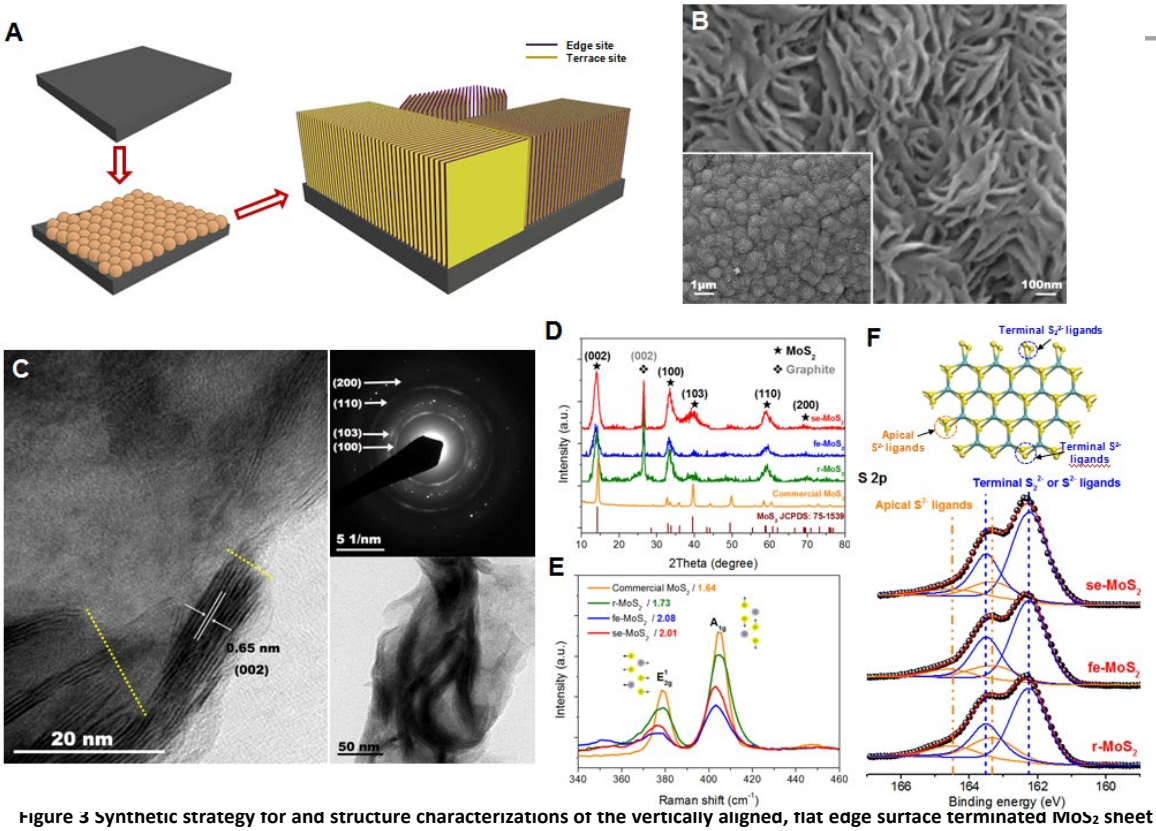

Figure 3 Synthetic strategy for and structure characterizations of the vertically aligned, flat edge surface terminated MoS_2 sheet arrays (fe-MoS_2). (**A**) Synthesis procedure of flat edge-terminated MoS_2 arrays (fe-MoS_2) via a microwave hydrothermal method. (**B**) High- and (inset) low-magnification FESEM images of fe-MoS_2, suggesting an edge-terminated vertically aligned morphology of MoS_2 nanosheet arrays on the substrate surface. (**C**) High- and low-magnification TEM images and (inset) the corresponding selected-area electron diffraction (SAED) patterns of fe-MoS_2. (**D**) XRD patterns of the r-MoS_2, fe-MoS_2, se-MoS_2 samples, commercial MoS_2, and the standard pattern of the pristine MoS_2 (JCPDS 75-1539). (**E**) Raman spectra of the r-MoS_2, fe-MoS_2, se-MoS_2 samples and commercial MoS_2. The higher relative intensity of the A_{1g} mode for fe-MoS_2 and se-MoS_2 samples suggests the edge-terminated surface structure. (**F**) S 2*p* XPS spectra and fitted peaks of r-MoS_2, fe-MoS_2 and se-MoS_2 samples. Decomposition of the S 2*p* region can be fitted with two district doublets ($2p_{3/2}$ and $2p_{1/2}$): one doublet (in blue) at about 162.3 ± 0.2 eV and 163.5 ± 0.2 eV, which reflects the terminal S_2^{2-} or S^{2-} ligands, the doublet (in orange) at about 163.1 ± 0.2 eV and 164.3 ± 0.2 eV, which reflects the apical S^{2-} ligands. The molecular structure depicted at the top of (**F**) is the schematic structure of MoS_2 crystal, where yellow and dark cyan spheres represent S and Mo atoms, respectively.

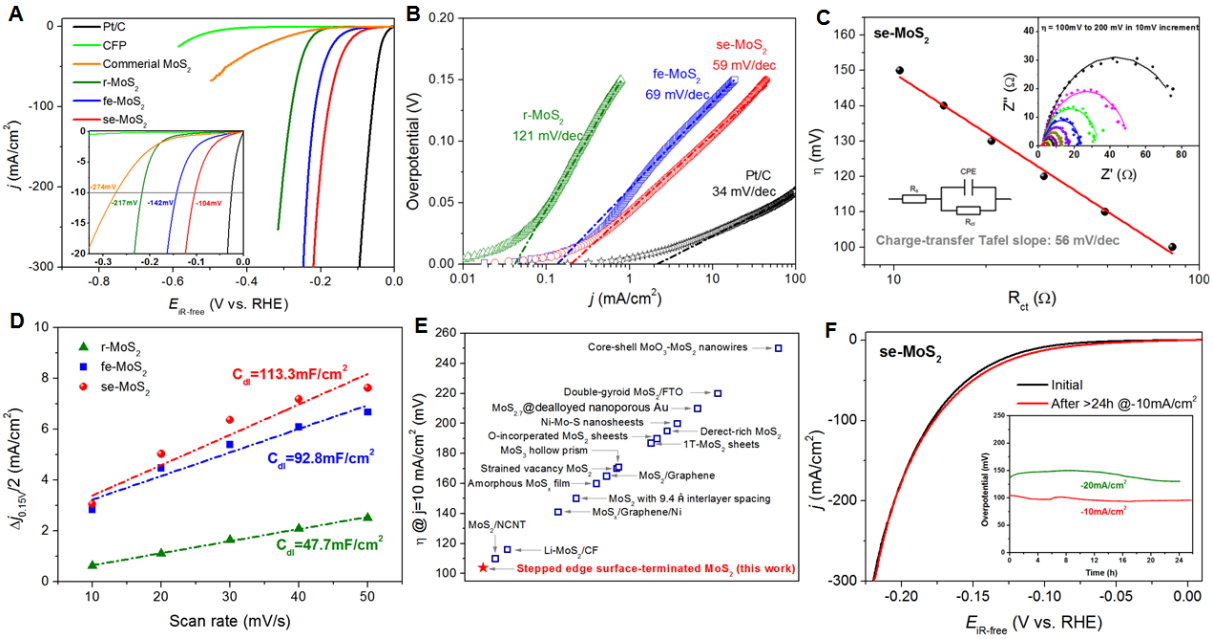

Figure 4 HER kinetics with different edge surface structures of MoS_2. (**A**) Polarization curves of the commercial MoS_2, r-MoS_2, fe-MoS_2 and se-MoS_2, and commercial Pt/C catalysts at a scan rate of 5 mV/s in 0.5M H_2SO_4 solution. (**B**) Tafel plots for the r-MoS_2, fe-MoS_2 and se-MoS_2, and commercial Pt/C catalysts derived from (A). (**C**) Charge-transfer Tafel plots of se-MoS_2 for the various catalysts derived from the Nyquist plots. Inset: Nyquist plots and fits of the impedance response of the vertically aligned MoS_2 sheet array catalyst under the overpotential from 100 mV to 200 mV in 10 mV increment, and the corresponding equivalent circuit that was used to fit the electrochemical impedance spectroscopy (EIS) data. (**D**) Charging current density differences plotted against scan rate of se-MoS_2, C_{dl} is equivalent to the slope of the fitted line. (**E**) Comparison of overpotential required to generate a current density of 10 mA/cm^2 on various MoS_2-based catalysts. (**F**) Polarization curves recorded from se-MoS_2 at a scan rate of 5 mV/s before (black curve) and after (red curve) the chronopotentiometry test at -10 mA/cm^2 > 24 h. Inset: chronopotentiometry responses ($\eta \sim t$) recorded from se-MoS_2 at high current densities of -10 mA/cm^2 and -20 mA/cm^2.

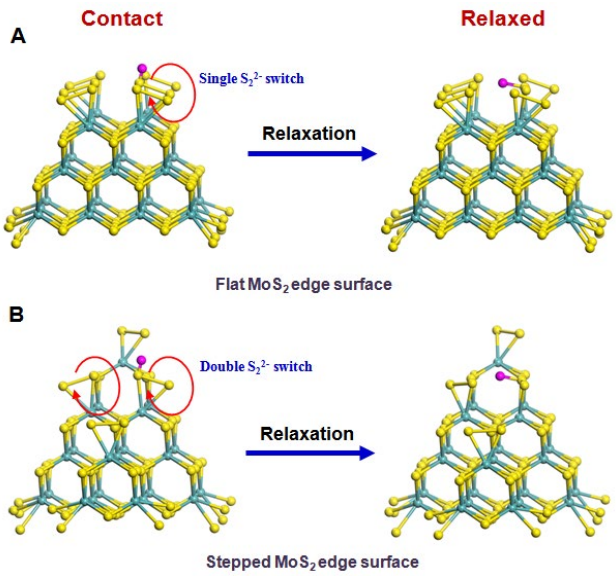

Figure 5 DFT-calculated potential relaxation process to stably absorb H on the disulfide ligands. Top view of the process contact and relaxed local structures of the (**A**) flat edge surface terminated MoS_2 (fe-MoS_2) system and (**B**) stepped edge surface terminated MoS_2 (se-MoS_2) system to stably absorb ¼ ML hydrogen on one of the MoS_2 layers, where violet, yellow and dark cyan spheres represent H, S and Mo atoms, respectively.